Anisotropy estimation of trabecular bone in gray-scale: comparison between cone beam and micro computed tomography data

Rodrigo Moreno, Magnus Borga, Eva Klintström, Torkel Brismar and Örjan Smedby

Abstract Measurement of anisotropy of trabecular bone has clinical relevance in osteoporosis. In this study, anisotropy measurements of 15 trabecular bone biopsies from the radius estimated by different fabric tensors on images acquired through cone beam computed tomography (CBCT) and micro computed tomog-

Rodrigo Moreno
Department of Radiology and Department of Medical and Health Sciences
Linköping University, Linköping, Sweden
Center for Medical Image Science and Visualization (CMIV)
Linköping University, Linköping, Sweden
Linköping University, Campus US, 581 85 Linköping, Sweden,
e-mail: rodrigo.moreno@liu.se

Magnus Borga
Department of Biomedical Engineering
Linköping University, Linköping, Sweden
Center for Medical Image Science and Visualization (CMIV)
Linköping University, Linköping, Sweden
e-mail: magnus.borga@liu.se

Eva Klintström
Department of Radiology and Department of Medical and Health Sciences
Linköping University, Linköping, Sweden
Center for Medical Image Science and Visualization (CMIV)
Linköping University, Linköping, Sweden
e-mail: eva.klintstrom@lio.se

Torkel Brismar
Department of Radiology,
Karolinska University Hospital at Huddinge, Huddinge, Sweden,
e-mail: torkel.brismar@gmail.com

Örjan Smedby
Department of Radiology and Department of Medical and Health Sciences
Linköping University, Linköping, Sweden
Center for Medical Image Science and Visualization (CMIV)
Linköping University, Linköping, Sweden
e-mail: orjan.smedby@liu.se

raphy (micro-CT) were compared. The results show that the generalized mean intercept length (MIL) tensor performs better than the global gray-scale structure tensor, especially when the von Mises-Fisher kernel is applied. Also, the generalized MIL tensor yields consistent results between the two scanners. These results suggest that this tensor is appropriate for estimating anisotropy in images acquired in vivo through CBCT.

Key words: Fabric tensors, CBCT, micro-CT, generalized MIL tensor, GST, Trabecular bone

1 Introduction

Fabric tensors aim at modeling through tensors both orientation and anisotropy of trabecular bone. Many methods have been proposed for computing fabric tensors from segmented images, including boundary-, volume-, texture-based and alternative methods (cf. [19] for a complete review). However, due to large bias generated by partial volume effects, these methods are usually not applicable to images acquired in vivo, where the resolution of the images is in the range of the trabecular thickness. Recently, different methods have been proposed to deal with this problem. In general, these methods directly compute the fabric tensor on the gray-scale image, avoiding in that way the problematic segmentation step.

Different imaging modalities can be used to generate 3D images of trabecular bone in vivo, including different magnetic resonance imaging (MRI) protocols and computed tomography (CT) modalities. The main disadvantages of MRI are that it requires long acquisition times that can easily lead to motion-related artifacts and that the obtained resolution with this technique is worse compared to the one obtained through CT in vivo [8]. Regarding CT modalities, cone beam CT (CBCT) [16, 22] and high-resolution peripheral quantitative CT (HR-pQCT) [1, 5] are two promising CT techniques for in vivo imaging. Although these techniques are not appropriate to all skeletal sites, their use is appealing since they can attain higher resolutions and lower doses than standard clinical CT scanners. CBCT has the extra advantages with respect to HR-pQCT that it is available in most hospitals in the western world, since it is used in clinical practice in dentistry wards, and, on top of that, the scanning time is shorter (30s vs. 3min), so it is less prone to motion artifacts than HR-pQCT.

As already mentioned, there are many methods available for computing tensors describing anisotropy in gray-scale [19]. A strategy for choosing the most appropriate method is to assess how similar the tensors computed from a modality for in vivo imaging (e.g., CBCT) are with respect to the ones computed from the reference imaging modality (micro-CT) for the same specimens. This was actually the strategy that we follow in this chapter.

From the clinical point of view, it seems more relevant to track changes in anisotropy than in the orientation of trabecular bone under treatment, since osteo-

porosis can have more effect on its anisotropy than on its orientation [23, 13]. Thus, the aim of the present study was to compare anisotropy measurements from different fabric tensors computed on images acquired through cone beam computed tomography (CBCT) to the same tensors computed on images acquired through micro computed tomography (micro-CT).

Due to its flexibility, we have chosen in this study our previously proposed generalized mean intercept length (MIL) tensor [17] (GMIL) with different kernels and, due to its simplicity, the global gray-scale structure tensor (GST) [26]. This chapter is an extended version of the work in [18].

The chapter is organized as follows. Section 2 presents the material and methods used in this study. Section 3 shows comparisons between using GMIL and GST in both CBCT and micro-CT data. Finally, Sect. 4 discusses the results and outlines our current ongoing research.

2 Material and methods

2.1 Material

The samples in this study consisted of 15 bone biopsies from the radius of human cadavers donated to medical research. The biopsies were approximately cubic with a side of 10 mm. Each cube included a portion of cortical bone on one side to facilitate orientation. The bone samples were placed in a test tube filled with water and the tube was placed in the centre of a paraffin cylinder, with a diameter of approximately 10 cm, representing soft tissue to simulate measurements in vivo. After imaging, a cube, approximately 8 mm in side, with only trabecular bone was digitally extracted from each dataset for analysis.

2.2 Image acquisition and reconstruction

The specimens were examined both with CBCT and with micro-CT. The CBCT data were acquired with a 3D Accuitomo FPD 80 (J.Morita Mfg. Corp., Kyoto, Japan) with a current of 8mA and a tube voltage of 85kV. The obtained resolution was 80 micrometers isotropic. The micro-CT data were acquired with a μCT 40 (SCANCO Medical AG, Bassersdorf, Switzerland) with a tube voltage of 70 kVp. The voxels have an isotropic resolution of 20 microns. Figure 1 shows slices and volume renderings of one of the imaged specimens.

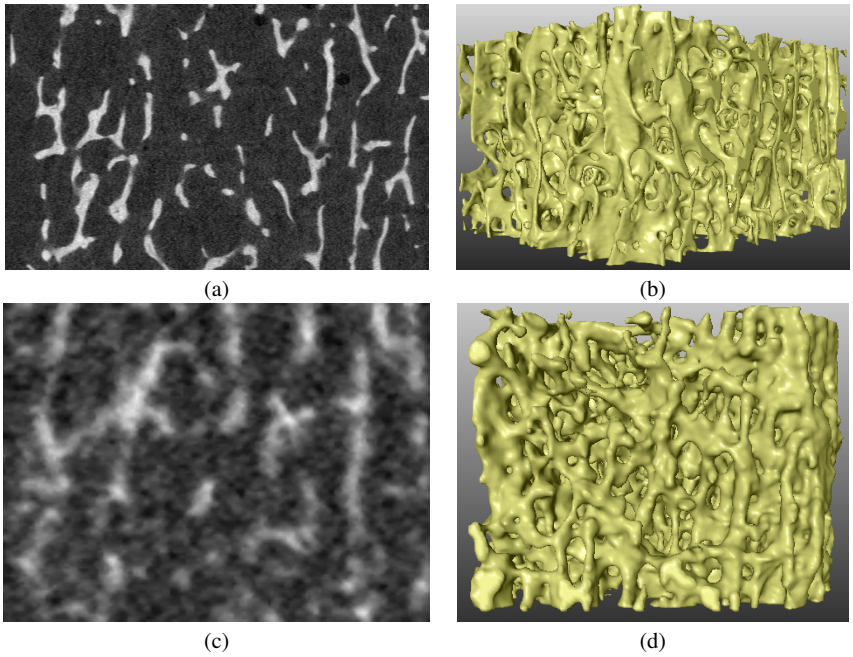

Fig. 1 Slices (left) and volume renderings (right) of one of the imaged specimens. Top: images acquired through micro-CT. Bottom: images acquired through CBCT.

2.3 Methods

The tensors were computed through the generalized MIL tensor (GMIL) and the GST.

2.3.1 GMIL tensor

Basically, the GMIL tensor is computed in three steps. The mirrored extended Gaussian image (EGI) [12] is computed from a robust estimation of the gradient. Second, the EGI is convolved with a kernel in order to obtain an orientation distribution function (ODF). Finally, a second-order fabric tensor is computed from the ODF. More formally, the generalized MIL tensor is computed as:

$$\mathsf{MIL} = \int_{\Omega} \frac{v\,v^T}{C(v)^2}\, d\Omega, \tag{1}$$

where v are vectors on the unitary sphere Ω, and C is given by:

$$C = H * E, \tag{2}$$

that is, the angular convolution ($*$) of a kernel H with the mirrored EGI E. Thanks to the Funk-Hecke theorem [9, 3], this convolution can be performed efficiently in the spherical harmonics domain when the kernel is positive and rotationally symmetric with respect to the north pole.

One of the advantages of the GMIL tensor is that different kernels can be used in order to improve the results. In this study, the half-cosine (HC) and von Mises-Fisher (vMF) kernels have been applied to the images. The HC has been selected since it makes equivalent the generalized and the original MIL tensor. The HC is given by:

$$H(\phi) = \begin{cases} \cos(\phi) & \text{,if } \phi \leq \pi/2 \\ 0 & \text{,otherwise,} \end{cases} \tag{3}$$

with ϕ being the polar angle in spherical coordinates. Moreover, the vMF kernel, which is given by [14]:

$$H(\phi) = \frac{\kappa}{4\pi \sinh(\kappa)} e^{\kappa \cos(\phi)}, \tag{4}$$

has been selected since it has a parameter κ that can be used to control its smoothing action. In particular, the smoothing effect is reduced as the values of κ are increased [17].

Figure 2 shows different kernels that can be used with the GMIL tensor. As already mentioned, these kernels must be positive and symmetric with respect to the north pole. As shown in the figure, the HC kernel is too broad (it covers half of the sphere), which can result in excessive smoothing. On the contrary, the impulse kernel is the sharpest possible kernel. As shown in [17], the GST makes use of the impulse kernel. In turn, the size of the smoothing effect of the vMF kernel can be controlled through the parameter κ. As shown in the figure, vMF is broader than the HC for small values of κ and it converges to the impulse kernel in the limit when $\kappa \to \infty$.

2.3.2 GST tensor

On the other hand, the GST computes the fabric tensor by adding up the outer product of the local gradients with themselves [26], that is:

$$\mathsf{GST} = \int_{p \in I} \nabla I_p \nabla I_p^T \, dI, \tag{5}$$

where I is the image and ∇I_p is the gradient.

Notice that GST related to the well-known local structure tensor (ST) which has been used in the computer vision community since 1980s [4]. There are different methods for computing ST, including quadrature filters [7], higher-order derivatives [15] or tensor voting [20]. However, the most used ST is given by:

$$\mathsf{ST}_\sigma(p) = G_\sigma * \nabla I_p \nabla {I_p}^T \tag{6}$$

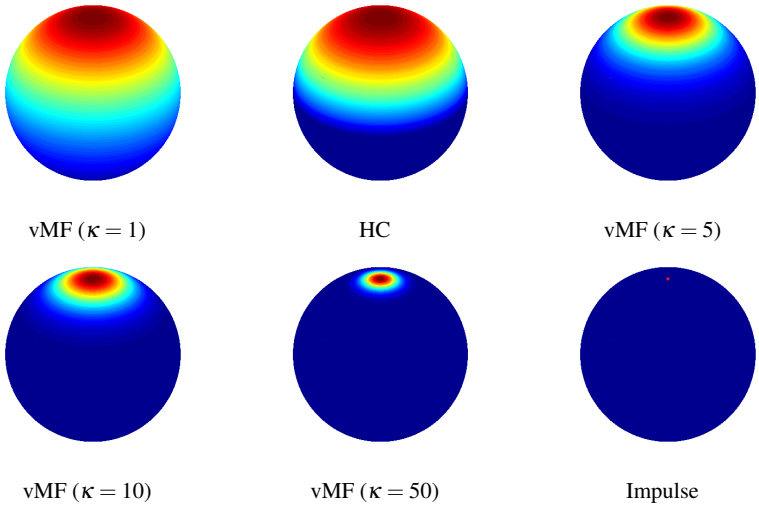

Fig. 2 Graphical representation of some kernels from the broadest to the narrowest, where zero and the largest values are depicted in blue and red respectively. Notice that the impulse kernel has been depicted as a single red dot in the north pole of the sphere.

where G_σ is a Gaussian weighting function with zero mean and standard deviation σ. In fact, ST becomes the GST when $\sigma \to \infty$. The main advantage of this structure tensor is that it is easy to code.

3 Results

As already mentioned, the focus in this chapter is the estimation of anisotropy. As a matter of fact, both the GMIL (and therefore the MIL tensor) and the GST tensors yield the same orientation information, since they have the same eigenvectors (cf. [17] for a detailed proof). This means that only the eigenvalues of the tensors are of interest for the purposes of this chapter.

The following three values have been computed for each tensor:

$$\begin{aligned} E1' &= E1/(E1+E2+E3) \\ E2' &= E2/E1, \\ E3' &= E3/E1, \end{aligned}$$

where E1, E2 and E3 are the largest, intermediate and smallest eigenvalues of the tensor. These three values have been selected since they are directly related to the shape of the tensor.

Table 1 Mean (SD) of E1' for fabric tensors computed on CBCT and micro-CT and the mean difference (SD) between both values. HC and vMF refer to the generalized MIL tensor, with the HC, and vMF kernels respectively. Parameter κ for vMF is shown in parenthesis. Positive and negative values of the difference mean over- and under estimations of CBCT with respect to micro-CT. All values have been multiplied by 100.

Tensor	micro-CT	CBCT	Difference
HC	44.65 (1.54)	42.38 (0.90)	2.25 (0.84)
vMF(1)	34.12 (0.29)	34.70 (0.18)	0.42 (0.15)
vMF(5)	51.55 (3.56)	47.07 (2.17)	4.51 (1.82)
vMF(10)	58.98 (4.63)	53.90 (3.21)	5.11 (2.13)
GST	45.69 (1.58)	44.79 (1.58)	0.90 (2.09)

Table 2 Mean (SD) of E2' for fabric tensors computed on CBCT and micro-CT and the mean difference (SD) between both values. HC and vMF refer to the generalized MIL tensor, with the HC, and vMF kernels respectively. Parameter κ for vMF is shown in parenthesis. Positive and negative values of the difference mean over- and under estimations of CBCT with respect to micro-CT. All values have been multiplied by 100.

Tensor	micro-CT	CBCT	Difference
HC	65.94 (5.85)	71.50 (3.53)	-6.11 (2.19)
vMF(1)	93.70 (1.69)	95.27 (1.02)	-1.84 (0.73)
vMF(5)	52.13 (9.54)	61.63 (6.53)	-8.48 (3.09)
vMF(10)	39.41 (9.74)	48.31 (7.75)	-8.96 (4.43)
GST	80.71 (10.66)	78.58 (7.66)	2.24 (7.41)

Table 3 Mean (SD) of E3' for fabric tensors computed on CBCT and micro-CT and the mean difference (SD) between both values. HC and vMF refer to the generalized MIL tensor, with the HC, and vMF kernels respectively. Parameter κ for vMF is shown in parenthesis. Positive and negative values of the difference mean over- and under estimations of CBCT with respect to micro-CT. All values have been multiplied by 100.

Tensor	micro-CT	CBCT	Difference
HC	58.29 (2.93)	65.18 (2.20)	-5.58 (2.98)
vMF(1)	91.09 (1.01)	92.92 (0.67)	-1.59 (0.89)
vMF(5)	42.72 (5.11)	51.20 (3.71)	-9.55 (4.49)
vMF(10)	31.17 (4.94)	37.81 (3.91)	-6.64 (2.70)
GST	38.71 (4.90)	44.96 (3.78)	-6.31 (4.40)

Tables 1-3 show the mean and standard deviation of E1', E2' and E3' computed on micro-CT and CBCT for the tested methods, and the mean difference and standard deviation between micro-CT and CBCT. As a general trend, the tested methods tend to overestimate E1' and underestimate E2' and E3' in CBCT. As shown, the best performance is obtained by vMF with κ =1 with small differences between tensors computed in both modalities. However, the tensors computed with this broad kernel are almost isotropic (cf. Tables 2 and 3), which makes it not suitable for detecting anisotropies in trabecular bone. It is also worthwhile to notice that the standard deviation of the differences increases with narrower kernels, such as GST. This means that a mild smoothing effect from middle range kernels such as vMF with κ=10, have a positive effect in the estimation of fabric tensors, since the dif-

ferences between micro-CT and CBCT are reduced while keeping the anisotropy of the tensors.

Table 4 shows the correlations between the measurements obtained on CBCT and micro-CT. Also, Figure 3 (left) shows the corresponding correlation plots for E1', E2' and E3' for HC, vMF (with κ = 10) and GST. It can be seen that the best correlations are yielded by vMF with different values of κ, and GST has a poor performance.

Table 4 Correlations between CBCT and micro-CT of E1', E2' and E3' of different fabric tensors. HC and vMF refer to the generalized MIL tensor, with the HC, and vMF kernels respectively. Parameter κ for vMF is shown in parenthesis. 95% confidence intervals are shown in parentheses.

Tensor	E1'	E2'	E3'
HC	0.90 (0.73;0.97)	0.91 (0.76;0.97)	0.67 (0.23;0.88)
vMF(1)	0.90 (0.72;0.97)	0.90 (0.73;0.97)	0.70 (0.29;0.89)
vMF(5)	0.91 (0.75;0.97)	0.91 (0.75;0.97)	0.80 (0.48;0.93)
vMF(10)	0.92 (0.76;0.97)	0.90 (0.72;0.97)	0.84 (0.57;0.94)
GST	0.51 (0.00;0.81)	0.71 (0.33;0.90)	0.51 (0.00;0.81)

Figure 3 (right) shows correlation plots of the three eigenvalues normalized by the sum of them for the same three methods. As shown in this figure, the tensors yielded by the three methods have different shapes. First, vMF with $\kappa = 10$ generates the most anisotropic tensors with larger differences between E1 and E2 than HC and GST. Second, HC generates the most isotropic tensors with smaller differences between values of E1, E2 and E3 than the other tensors. Finally, unlike GST, both HC and vMF generate tensors that are close to be orthotropic, that is, E2 $\approx$ E3. This is in line with the common assumption of orthotropy for trabecular bone [28].

Figures 4-6 show Bland-Altman plots for the generalized MIL tensor with the HC and vMF (with κ=10) kernels and the GST. As seen in these figures, GST yields wider limits of agreement, i.e., larger discrepancies between CBCT and micro-CT, than HC and vMF, in particular for E2' and E3'. One of the advantages of using the vMF kernel is that its parameter can be adjusted in order to improve the correlations between CBCT and micro-CT. Figure 7 shows the evolution of the correlations between CBCT and micro-CT with the parameter κ of the generalized MIL tensor with the vMF kernel. From this figure, E1' and E2' attain their maxima at κ = 10, κ = 5 respectively, while E3' asymptotically approaches a correlation of 0.875 when $\kappa \to \infty$. Since the three measurements determine the shape of the tensor, we suggest to choose the value of κ that maximizes the three correlations, that is, that maximizes (E1'+E2'+E3')/3. In our case, such a value is $\kappa = 10$, as is also shown in Fig. 7.

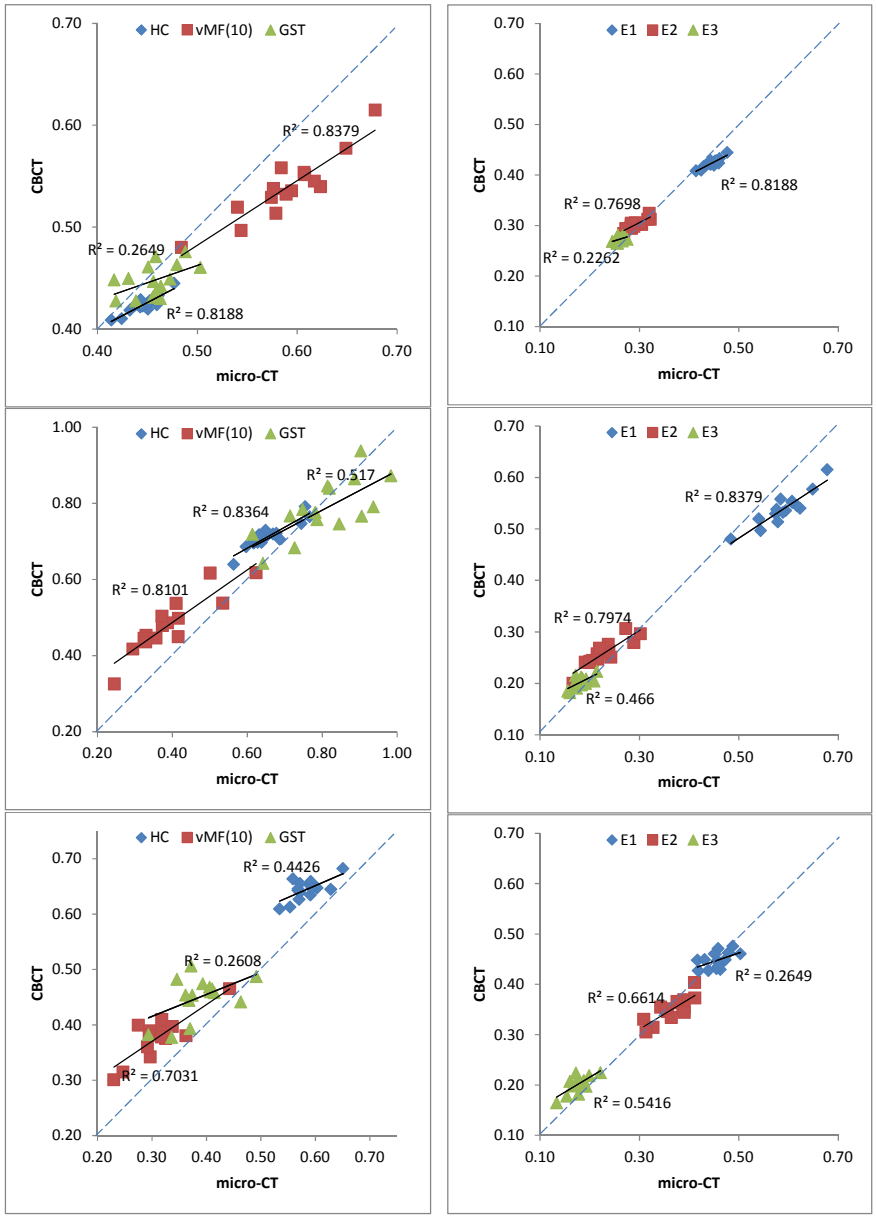

Fig. 3 Left: correlation plots for E1' (top), E2' (middle) and E3' (bottom) between CBCT and micro-CT for HC, vMF ($\kappa = 10$) and GST. Right: correlation plots for HC (top), vMF (κ=10) (middle) and GST (bottom) between CBCT and micro-CT for the three eigenvalues normalized by the sum of them.

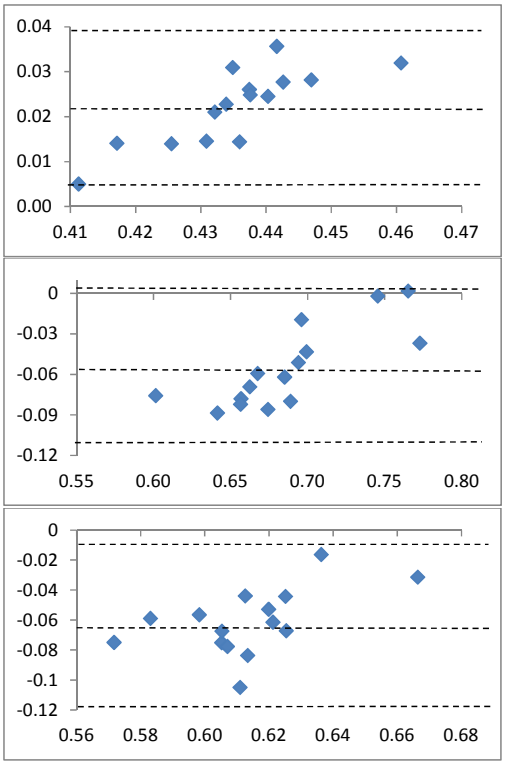

Fig. 4 Bland-Altman plots for E1' (top), E2' (middle) and E3' (bottom) between CBCT and micro-CT for HC. The vertical and horizontal axes show the measurements on micro-CT minus those computed on CBCT, and the mean between them respectively. The mean difference and the mean difference $\pm$ 1.96 SD are included as a reference in dotted lines.

4 Discussion

We have compared in this chapter the anisotropy of different fabric tensors estimated on images acquired through CBCT and micro-CT of 15 trabecular bone biopsies from the radius. The results presented in the previous section show strong correlations between micro-CT and CBCT for the generalized MIL tensor with HC and vMF kernels, especially with $\kappa = 10$. In addition, good agreements between measurements in CBCT and the reference micro-CT have been shown through Bland-Altman plots for HC, vMF with $\kappa = 10$ and GST. An interesting result is that the GST yields clearly lower correlation values than the generalized MIL tensor using either HC or vMF kernels. We have shown that the GST can be seen as a variant of the generalized MIL tensor where the impulse kernel is applied instead of the HC [17].

In this line, the results from the previous section suggest that the use of broader smoothing kernels such as HC or vMF has a positive effect for increasing the corre-

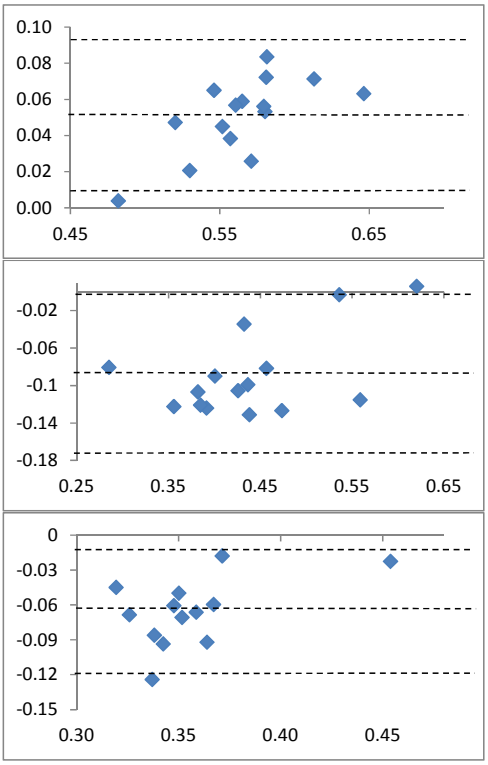

Fig. 5 Bland-Altman plots for E1' (top), E2' (middle) and E3' (bottom) between CBCT and micro-CT for vMF with κ=10. The vertical and horizontal axes show the measurements on micro-CT minus those computed on CBCT, and the mean between them respectively. The mean difference and the mean difference $\pm$ 1.96 SD are included as a reference in dotted lines.

lation of the tensors computed on images acquired through suitable scanners for in vivo with the ones that can be computed from images acquired in vitro. Although the three tested methods yield tensors that share their eigenvectors, their eigenvalues are different, as shown in Figure 3, which is a natural consequence of using different smoothing kernels. Moreover, the high correlations reported for HC and vMF enable to eliminate of the systematic errors reported in Tables 1-3 and in the Bland-Altman plots for these two types of fabric tensors.

Another interesting observation is that vMF yielded better results than the standard HC. This means that κ can be used to tune the smoothing in such a way that the results are correlated with in vitro measurements. For the imaged specimens, a value of $\kappa = 10$ yielded the best correlation results.

The results presented in this chapter suggest that advanced fabric tensors are suitable for in vivo imaging, which opens the door to their use in clinical practice. In particular, the results show that the generalized MIL tensor is the most promising option for use in vivo. As shown in this chapter, this method is advantageous since

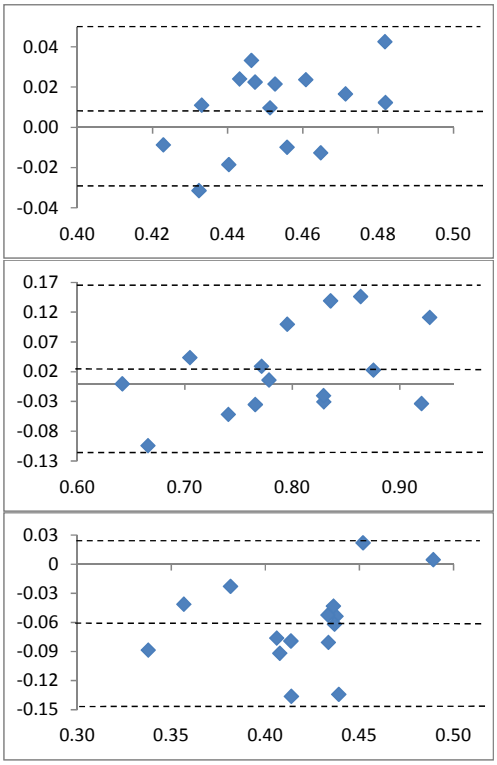

Fig. 6 Bland-Altman plots for E1' (top), E2' (middle) and E3' (bottom) between CBCT and micro-CT for GST. The vertical and horizontal axes show the measurements on micro-CT minus those computed on CBCT, and the mean between them respectively. The mean difference and the mean difference $\pm$ 1.96 SD are included as a reference in dotted lines.

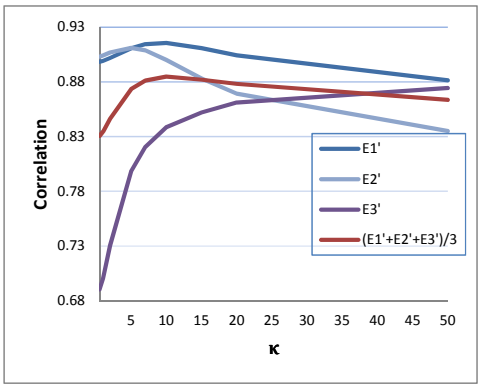

Fig. 7 Evolution of the correlations between CBCT and micro-CT with the parameter κ of the generalized MIL tensor with the vMF kernel.

it has the possibility to improve its performance by changing the smoothing kernel by a more appropriate one, as it was shown in this chapter for the vMF kernel.

A poor performance of the GST has also been reported in images acquired through multi-slice computed tomography (MSCT) [25]. The authors of that study hypothesized that such a bad performance could be due to voxel anisotropy obtained from MSCT. However, the results from the current study suggest that the problems of the GST are more structural, since they are also present in CBCT with isotropic voxels. Thus, the problems of GST seem more related to the applied kernel (the impulse kernel) than to the voxel anisotropy of the images.

Ongoing research includes performing comparisons in different skeletal sites, different degrees of osteoporosis and comparing the results with images acquired through HR-pQCT and micro-MRI [11, 6]. Furthermore, relationships between fabric and elasticity tensors will be explored. The MIL tensor has extensively been used for predicting elasticity tensors in trabecular bone [2, 27, 10]. However, since the GMIL with the vMF kernel has a better performance than the MIL tensor for reproducing in vitro measurements, we want to investigate whether or not the GMIL tensor can also be used to increase the accuracy of the MIL tensor for predicting the elastic properties of trabecular bone.

In the same line, we have recently hypothesized that trabecular termini (i.e., free ended trabeculae [24]) should not be considered for computing fabric tensors since contribution of termini to the mechanical competence of trabecular bone is rather limited [21]. Thus, it is worthwhile to assess the power of fabric tensors that disregard termini for predicting elasticity.

Acknowledgements We thank Andres Laib from SCANCO Medical AG for providing the micro-CT data of the specimens. The authors declare no conflict of interest.

References

1. Burghardt, A., Link, T., Majumdar, S.: High-resolution computed tomography for clinical imaging of bone microarchitecture. Clinical Orthopaedics and Related Research **469**(8), 2179–2193 (2011)
2. Cowin, S.: The relationship between the elasticity tensor and the fabric tensor. Mechachics of Materials **4**(2), 137–147 (1985)
3. Driscoll, J.R., Healy, D.M.: Computing Fourier transforms and convolutions on the 2-sphere. Advances in Applied Mathematics **15**(2), 202–250 (1994)
4. Förstner, W.: A feature based correspondence algorithm for image matching. In: The International Archives of the Photogrammetry and Remote Sensing, vol. 26, pp. 150–166 (1986)
5. Geusens, P., Chapurlat, R., Schett, G., Ghasem-Zadeh, A., Seeman, E., de Jong, J., van den Bergh, J.: High-resolution in vivo imaging of bone and joints: a window to microarchitecture. Nature Reviews Rheumatology (2014). In press
6. Gomberg, B., Wehrli, F., Vasili'c, B., Weening, R., Saha, P., Song, H., Wright, A.: Reproducibility and error sources of -mri-based trabecular bone structural parameters of the distal radius and tibia. Bone **35**(1), 266 – 276 (2004)
7. Granlund, G.H., Knutsson, H.: Signal Processing for Computer Vision. Kluwer Academic Publishers, Dordrecht The Netherlands (1995)

8. Griffith, J., Genant, H.: New advances in imaging osteoporosis and its complications. Endocrine **42**, 39–51 (2012)
9. Groemer, H.: Geometric applications of Fourier series and spherical harmonics. Cambridge University Press (1996)
10. Gross, T., Pahr, D., Zysset, P.: Morphology-elasticity relationships using decreasing fabric information of human trabecular bone from three major anatomical locations. Biomechanics and Modeling in Mechanobiology **12**(4), 793–800 (2013)
11. Hipp, J., Jansujwicz, A., Simmons, C., Snyder, B.: Trabecular bone morphology from micromagnetic resonance imaging. Journal of Bone Mineral Research **11**(2), 286–297 (1996)
12. Horn, B.K.P.: Extended Gaussian images. Proceedings of the IEEE **72**(12), 1671–1686 (1984)
13. Huiskes, R.: If bone is the answer, then what is the question? Journal of Anatomy **197**, 145–156 (2000)
14. Jupp, P.E., Mardia, K.V.: A unified view of the theory of directional statistics, 1975-1988. International Statistics Review **57**(3), 261–294 (1989)
15. Köthe, U., Felsberg, M.: Riesz-transforms versus derivatives: On the relationship between the boundary tensor and the energy tensor. In: Scale Space and PDE Methods in Computer Vision, Hofgeismar Germany, *LNCS*, vol. 3459, pp. 179–191 (2005)
16. Monje, A., Monje, F., Gonzalez-Garcia, R., Galindo-Moreno, P., Rodriguez-Salvanes, F., Wang, H.: Comparison between microcomputed tomography and cone-beam computed tomography radiologic bone to assess atrophic posterior maxilla density and microarchitecture. Clinical Oral Implants Research pp. 1–6 (2013)
17. Moreno, R., Borga, M., Smedby, Ö.: Generalizing the mean intercept length tensor for gray-level images. Medical Physics **39**(7), 4599–4612 (2012)
18. Moreno, R., Borga, M., Smedby, Ö.: Correlations between fabric tensors computed on cone beam and micro computed tomography images. In: J. Tavares, R. Natal-Jorge (eds.) Computational Vision and Medical Image Processing (VIPIMAGE), pp. 393–398. CRC Press (2013)
19. Moreno, R., Borga, M., Smedby, Ö.: Techniques for computing fabric tensors: a review. In: B. Burgeth, A. Vilanova, C.F. Westin (eds.) Visualization and Processing of Tensors and Higher Order Descriptors for Multi-Valued Data. Springer (2014). In press
20. Moreno, R., Pizarro, L., Burgeth, B., Weickert, J., Garcia, M.A., Puig, D.: Adaptation of tensor voting to image structure estimation. In: D. Laidlaw, A. Vilanova (eds.) New Developments in the Visualization and Processing of Tensor Fields, pp. 29–50. Springer (2012)
21. Moreno, R., Smedby, Ö.: Volume-based fabric tensors through lattice-Boltzmann simulations. In: Proceedings International Conference on Pattern Recognition (ICPR), Stockholm Sweden (2014). Accepted
22. Mulder, L., van Rietbergen, B., Noordhoek, N.J., Ito, K.: Determination of vertebral and femoral trabecular morphology and stiffness using a flat-panel C-arm-based CT approach. Bone **50**(1), 200–208 (2012)
23. Odgaard, A., Kabel, J., van Rietbergen, B., Dalstra, M., Huiskes, R.: Fabric and elastic principal directions of cancellous bone are closely related. Journal of Biomechanics **30**(5), 487–495 (1997)
24. Tabor, Z.: Novel algorithm detecting trabecular termini in μCT and MRI images. Bone **37**(3), 395–403 (2005)
25. Tabor, Z., Petryniak, R., Latała, Z., Konopka, T.: The potential of multi-slice computed tomography based quantification of the structural anisotropy of vertebral trabecular bone. Medical Engineering & Physics **35**(1), 7 – 15 (2013)
26. Tabor, Z., Rokita, E.: Quantifying anisotropy of trabecular bone from gray-level images. Bone **40**(4), 966–972 (2007)
27. Zysset, P.K.: A review of morphology-elasticity relationships in human trabecular bone: theories and experiments. Journal of Biomechanics **36**(10), 1469–1485 (2003)
28. Zysset, P.K., Goulet, R.W., Hollister, S.J.: A global relationship between trabecular bone morphology and homogenized elastic properties. Journal of Biomechanical Engineering **120**(5), 640–646 (1998)